# Electronic and hyperbolic dielectric properties of $ZrS_2/HfS_2$ Heterostructures

Liwei Zhang[1], Weiyang Yu[1], Qin Wang[1], Jun-Yu Ou[2], Baoji Wang[1,3], Gang Tang[4], Xingtao Jia[1], Xuefeng Yang[1], Guodong Wang[1], Xiaolin Cai[1]*

1 School of Physics and Electronic Information Engineering, Henan Polytechnic University, Jiaozuo, Henan 454000, P.R. China

2 Optoelectronics Research Centre & Centre for Photonic Metamaterials, University of Southampton, Southampton, SO17 1BJ, UK

3 School of Physics Science and Engineering, Tongji University, Shanghai, 200092, P. R. China

4 Theoretical Materials Physics, CESAM, Université de Liège, Liège, Belgium

* caixiaolin@hpu.edu.cn

**Abstract**- In this paper we investigate the electronic and optical dielectric properties of lateral and vertical heterostructures composed of two-dimensional (2D) $ZrS_2$ and $HfS_2$ monolayers based on density functional theory. First, we show that the bulk and monolayer $ZrS_2$ and $HfS_2$ as well as the vertical $(ZrS_2)_m/(HfS_2)_n$ heteroestructures are indirect band gap semiconductors, while the lateral heterostructures exhibit an indirect to direct bandgap transition. Then we demonstrate that the optical properties of the bulk and monolayer $HfS_2$ and $ZrS_2$ are strongly anisotropic, for the bulk $HfS_2$ and $ZrS_2$, the in-plane components of the dielectric function is negative in a certain frequency band, where they can work as naturally hyperbolic metamaterials (HMMs). Interestingly, the vertical heterostructures also possess a hyperbolic region, whose position and width can be tunable with the thickness ratio of constituents. It is also found that the $(ZrS_2)/(HfS_2)$ vertical heterostructures can enhance spontaneous emission and about 100-fold improvement of the Purcell factor is obtained. These results prove the feasibility of 2D material heterostructures to realize tunable hyperbolic metamaterials, the heterostructures present a promising opportunity for the practical applications in light-generation technologies.

PACS number(s): 71.20.-b, 73.21.-b,78.20.ci, 52.25.Os

## 1. Introduction

Two-dimensional (2D) materials, such as graphene, hexagonal boron-nitride (hBN), and the transition-metal dichalcogenides (TMDs) are presently being intensively researched because of their remarkable electronic, optical, mechanical and thermal properties [1-4]. Particularly, bulk TMDs, with the chemical formula $MX_2$ (M = Ti, Zr, Hf, Mo or W; X = S, Se, Te), are a class of important layered materials, in which transition metal atom M and chalcogen atoms X form X-M-X-type sandwich layers by strong intralayer chemical bonding and much weaker interlayer van der Waals (vdW) type interactions[5]. 2D monolayer TMDs display a rich physics and hold promise for a wide range of applications in flexible electronics, optoelectronics, energy storage, catalysis or spintronics [1,4,6]. At low temperature, some monolayer TMDs can be a 2D superconductor with coexisting charge-density wave [7]. In recent years, a variety of heterostructures have also been fabricated through the vertical or lateral combination of single layer or multilayer TMDs with other TMDs or with other 2D materials such as *h*-BN or graphene [2, 8-11]. TMDs-based heterostructures assembled for various electronic, optoelectronic, and photovoltaic applications have been theoretically and experimentally studied [12,13]. Some 2D heterostructured electrodes could

greatly expand current energy storage technologies [12], while TMDs-based heterostructures such as black phosphorus/TMDs have been predicted to be strong absorbers of light and suitable materials for excitonic thin-film solar cell applications [13]. Recently fabricated Zirconium disulfide ($ZrS_2$) and Hafnium disulphide ($HfS_2$) exhibit well-balanced carrier mobility and band gaps, and attracted interest in solar cells and field effect transistors [14-16]. Meanwhile, they show highly anisotropic mechanical, optical, and electrical properties [5,17]. More importantly, the layered TMDs can be naturally hyperbolic materials (HMMs) [18].

Hyperbolic metamaterials usually have negative permittivity in at least one direction, electromagnetic waves propagating through them undergo a transition from closed elliptical to open hyperbolic dispersions in corresponding frequency [19,20]. The hyperbolic dispersion enables unique metamaterial states with large magnitude wavevectors which are evanescent and decay exponentially in conventional media. As a matter of fact, HMMs offer great flexibility in tailoring the near-field distribution, which facilitates prospective applications in spontaneous emission enhancement [21], sub-wavelength imaging [20] and broadband absorption [22]. In particular, the important consequence of unbounded dispersion of HMM is a divergent local density of photonic states (LDOS), which results in an enhancement in the spontaneous emission of a dipole emitter placed in the vicinity of HMM and that leads to a HMM-based broadband Purcell effect [23]. HMMs can be realized at optical frequencies using periodically arranged metal-dielectric multilayers and metallic nanowire arrays, where the unit cells are much smaller than the operation wavelength [24]. However the performance of the metal-based HHM is limited by the finite size of the metallic components. Recently, a few 2D materials have been reported to exhibit hyperbolic dispersion in their pristine form. 2D materials such as $Bi_2Te_3$ [25], *h*-BN [26], while graphite [27], black phosphorene [28] as well as $ZrS_2$ and $HfS_2$ [5] present hyperbolic dispersion in the UV and near-IR to visible spectral ranges. Naturally hyperbolic materials, composed of "individual layers" on the atomic scale, have been seen to curtail the limitations of the finite size of the unit cell prevalent in artificial hyperbolic structures. Containing no internal interfaces for the electrons to scatter off, they possess an obvious advantage over traditional metamaterials. In experiments, single or few-layer nanosheets of these TMDs can be obtained by using Scotch-tape based micromechanical cleavage [29], CVD method, etc. [2]. In addition, many fabrication methods can be used to realized the lateral and vertical heterostructures as reviewed in Ref. [2, 30]. In this paper we investigate the electronic and the tunable hyperbolic optical property of the periodic lateral and vertical heterostructures composed of single or multilayer $ZrS_2$ and $HfS_2$ based on density functional theory (DFT). Finally, the

spontaneous emission enhancement of the heterostructure-based HMMs is also calculated.

**2. Models and computational details**

Considering the particularity of the 2D structures, there are two approaches for creating 2D heterostructures: the vertical (out-plane) and lateral (in-plane) types. In this paper, we present a theoretical study of lateral and vertical heterostructures made of nearly lattice matched single or multilayer 1T-$ZrS_2$ and 1T-$HfS_2$. 1T-$ZrS_2$ and 1T-$HfS_2$ are new types of 2D TMDs, which have the $CdI_2$ structure with $p\bar{3}m1$ space group. The vertical type, also known as vdW heterostructure is commonly achieved by stacking multiple monolayers vertically layer-by-layer [31]. In contrast to the vertical heterostructures (VHs), the interfaces in lateral heterostructures (LHs) are reduced from 2D to 1D, finally becoming an 'interline'[32]. The periodically repeating, lateral, and commensurate junctions of semiconducting $ZrS_2$ and $HfS_2$ stripes along their zigzag edge make a class of new materials [33]. Throughout this paper, these zigzag edged LHs are referred to as $(ZrS_2)_m$-$(HfS_2)_n$, where the indices *m* and *n* represent the numbers of each kind of building constituents in the lateral primitive unit cell. The VHs are constructed from the stacking of single or few $ZrS_2$ and $HfS_2$ layers, which are specified as $(ZrS_2)_m/(HfS_2)_n$. Because of the weak vdW interlayer interaction, the coupling between adjacent $ZrS_2$ and $HfS_2$ vertically stacked is rather weak, and it has small but crucial effects on the electronic structure [34]. The atomic configurations of the lateral and vertical heterostructures here proposed are sketched in Fig. 3 and Fig.S3 respectively.

All the calculations are performed based on DFT in conjunction with the projector augmented wave (PAW) potentials [35] implemented by the Vienna Ab initio Simulation Package code [36]. The exchange-correlation energy is described by the generalized gradient approximation using the Perdew-Burke-Ernzerhof (PBE) functional [37]. The periodic in-plane and out-plane hybridized layers are optimized within one repeating unit. The kinetic energy cutoff for the plane wave basis set was chosen to be 500eV and the convergence criteria for energy and force are set to be $10^{-5}$eV and 0.01eV/Å, respectively. We used the conjugate gradient method for optimizing the atomic positions, interlayer spacings, and lattice constants. Brillouin zones were sampled using the Monkhorst-Pack scheme [38] where the Gamma-centered k-point mesh is employed according to the size of unit cells in the direct space. The number of the k points along the in-plane periodic direction was determined by the smallest integer that fulfills $n_kL = 30$ Å, where L is the lattice constant of the supercell in the periodic direction. DFT-D2 method is applied to describe the long-range vdW interaction [39] for the VHs, which is important in determining the geometric and electronic

properties. The LHs and finite VHs are repeated periodically along the z-direction, a vacuum spacing of 18Å is introduced to avoid possible interactions between adjacent layers and their periodic images. Optical properties are some of the most important properties for a material, indicating a material's response to electromagnetic radiation. To model the optical response of the $ZrS_2$-$HfS_2$ heterostuctures, the complex dielectric function, $\varepsilon(\omega) = \varepsilon_1(\omega) + i\varepsilon_2(\omega)$, are calculated. The dielectric function provides a fundamental insight for evaluating further optoelectronic applications, since it connects the macroscopic properties with the microscopic band structure. The frequency or energy dependent dielectric function consists mainly of interband contributions for a semiconductor. The frequency dependent dielectric matrix contains the imaginary part of dielectric constants $\varepsilon_2(\omega)$ in PAW methodology would be obtained after the electronic ground state is determined [40]. Then the real part of the dielectric function can be obtained by the usual Kramers–Kronig transformation [41].

## 3. Results and discussions

### 3.1 Electronic properties

The 1T-$ZrS_2$ and 1T-$HfS_2$ consist of a layer of Zr (Hf) atoms sandwiched between two layers of S atoms with the Zr (Hf) atom octahedrally coordinated with the chalcogen one as shown in Fig. 1. The intralayer Zr (Hf)-S bonding is strong while the interlayer bonding is weak as it arises from vdW interaction. 1T-$ZrS_2$ and 1T-$HfS_2$ are all semiconductors and the band gaps fall in the range of the visible-infrared region, thus being promising candidates for photovoltaic applications [14]. The calculated lattice constants of bulk (monolayer) $ZrS_2$ and $HfS_2$ are a=b=3.6822 Å and a=b=3.642 Å (3.6821 Å and 3.643 Å), respectively, agreeing well with previous studies [33, 42]. The lattice mismatch of $ZrS_2$ and $HfS_2$ is merely 1.0%, implying that it is very suitable to build VHs and LHs based upon these two materials. For a better understanding of the electronic properties and the dielectric function of the $ZrS_2$/$HfS_2$ heterostructsures, it is useful to study the electronic structures of bulks and monolayer $ZrS_2$ and $HfS_2$. It is known that there is some difference in Brillouin zones of bulk and monolayer structures. The Brillouin zones with high symmetry k-points used in band structure calculations are illustrated in Fig. 1. As can be seen in Fig. 2 (a) and (b), the band gaps of bulk $ZrS_2$ and $HfS_2$ are both found to be indirect with values of 1.112 eV and 1.238 eV at PBE level, respectively, The valence band maximum (VBM) and conduction band minima (CBM) of the pristine bulk $ZrS_2$ and $HfS_2$ are located at Γ and L points, respectively. Fig.2 (c) and (d) are the band structures of the monolayer $ZrS_2$ and $HfS_2$. Clearly, they also belong to indirect band gap semiconductors with band gaps of 1.186 eV and

1.316 eV, respectively. Their CBM at Γ and VBM at M points, this feature is different from some other TMDs such as $MoS_2$, $WS_2$, et al, which undergo a transition from an indirect to direct gap semiconductor when their thickness is thinned down to a single layer [43].

Lateral and vertical heterostructures made of 2D single layer like Graphene/hBN [44] or $MoS_2/WS_2$[10] have been previously studied both, theoretically and experimentally, motivating the construction of composite materials with promising applications. The 1T-$ZrS_2$ and 1T-$HfS_2$ monolayers reported here possess hexagonal symmetry and a sandwich-like structure, with close lattice constants values. The similar geometric structures and lattice parameters of $ZrS_2$ and $HfS_2$ will be beneficial in experimental fabrications. Based on the structural characteristics, two different types of LHs can be established with zigzag and with armchair types of interlines. The $(ZrS_2)_m$-$(HfS_2)_n$ LHs with zigzag interlines are thermally and dynamically stable, the stable properties can be seen from the phonon dispersion and the molecules dynamic simulation as shown in Fig. S1(a) and (b) (see the Supplemental Material [45]). The frequencies of all phonon branches in the entire Brillouin zone are positive and the variation of free energy only shows slight oscillation even at 500 K. while the $(ZrS_2)_m$-$(HfS_2)_n$ LHs with armchair interlines are dynamically instable [33]. Therefore, in this paper we just focus on the $(ZrS_2)_m$-$(HfS_2)_n$ LHs with zigzag interlines. Fig. 3(a) shows the typical atomic structures of the zigzag LHs $(ZrS_2)_m$-$(HfS_2)_n$ , where $m$=$n$=6 are the numbers of formula units in the lateral primitive unit cell. The green, sand and yellow balls indicate Zr, Hf, and S atoms, respectively. Along the y-direction of the lateral heterostructures shown in Fig.3 (a), the monolayer $ZrS_2$ and $HfS_2$ extend to infinity. The x-direction is perpendicular to the zigzag edges, along which two different stripes repeat alternately and periodically. In the *xy*-plane, the heterostructure has a 2D rectangular lattice and each constituent consists of three parallel atomic planes, where the plane of metal atoms (Zr or Hf) is capped by two S atomic planes. The lateral heterostructures are repeated periodically along the z-direction with a vacuum spacing of 18 Å in a three-dimensional (3D) orthorhombic lattice. The proposed structure is similar to the previous h-BN/graphene, $MoS_2/WS_2$ and As/Sb based LHs [44, 46, 47]. Fig.3 (b) shows the 2D Brillouin zone of the monolayers with high symmetry points.

Among the lateral heterostructures, we first study the electronic structure of the $(ZrS_2)_1$-$(HfS_2)_1$ LH with zigzag interline, which is a composite structure constructed of very narrow stripes. As can be seen from the corresponding band structure plotted in Fig. 4(a), the $(ZrS_2)_1$-$(HfS_2)_1$ LH is a semiconductor with an indirect gap of 1.195 eV. In order to gain comprehensive information about $(ZrS_2)_m$-$(HfS_2)_n$ LHs, the size of building

stripes is further increased. In Fig. 4(b)-(e), we show the corresponding band structures of $(ZrS_2)_2$-$(HfS_2)_2$, $(ZrS_2)_3$-$(HfS_2)_3$, $(ZrS_2)_6$-$(HfS_2)_6$, and $(ZrS_2)_9$-$(HfS_2)_9$ LHs, respectively. An obvious common feature of this compounds is its direct band gap, with the VBM and CBM both located at the Γ point, displaying a rather different behavior from those of pristine bulk (monolayer) $ZrS_2$ and $HfS_2$ as well as $(ZrS_2)_1$-$(HfS_2)_1$. At PBE level, the calculated bandgaps of $(ZrS_2)_2$-$(HfS_2)_2$, $(ZrS_2)_3$-$(HfS_2)_3$, $(ZrS_2)_6$-$(HfS_2)_6$, and $(ZrS_2)_9$-$(HfS_2)_9$ LHs are 1.212 eV, 1.188 eV, 1.143 eV and 1.125 eV, respectively. There is a monotonous trend in the bandgap of $(ZrS_2)_m$-$(HfS_2)_n$ LHs, which decreases gradually as the width of $ZrS_2$ and $HfS_2$ constituents increase. To further check the direct nature, we also perform calculations at the more accurate but computationally expensive hybrid functional level [48]. As shown in Fig.S2 (a), the band gap of $(ZrS_2)_3$-$(HfS_2)_3$ LH is 2.008eV under the HSE06 correction, which also clearly suggests a direct bandgap feature for $(ZrS_2)_3$-$(HfS_2)_3$ LH. We found that the HSE functional only enlarges the band gaps moderately compared with the PBE but does not change the trend of the electronic structures. Although the quantitative accuracy is subject to some uncertainty, DFT methods are still powerful for predicting a correct trend and related physical mechanisms.

To discuss the origination of the indirect-direct band gap transition, we compare the two Brillouin zones shown in Fig.1 and Fig.3(b). It is found that the high-symmetry k-points Γ and M of the hexagonal phase would be folded into the Γ point in the new Brillouin zone of the rectangular supercell phase, thereby rendering $ZrS_2$ with its rectangular supercell structure $(ZrS_2)_2$-$(ZrS_2)_2$ as a (pseudo)-direct band gap material as shown in the left panel of Fig.S2(b). For the sake of comparison, the band structures of $(ZrS_2)_2$-$(HfS_2)_2$ are also plotted. We identify that band folding effect plays a critical role to produce the direct band gaps in the proposed LHs. In order to understand the electronics structures of the LHs, the projected band structures of $(ZrS_2)_3$-$(HfS_2)_3$ are plotted in Fig. 4(c). It is clear that the conduction band and the valence band mainly consist of states from $ZrS_2$and $HfS_2$, respectively, indicating the type-II heterostructure. The type-II band alignment could also be the reason for the transition from indirect to direct semiconductor in the LHs[33]. The plane-averaged electron density difference along the direction perpendicular to the 1D boundary and the charge density difference of the interface region are plotted in in Fig.S2 (c) to illustrate the bonding feature and charge transfer at the interface. It is found that the charge redistribution mainly involves the atoms near the 1D interface, where certain electrons transfer happens between the $HfS_2$ and $ZrS_2$ monolayer. In the LHs, the charge transfer is mainly related to the building components, as well as the interline between $HfS_2$ and

$ZrS_2$, leading to the presented orbital structure of bands in LHs.

Besides the lateral heterostructures, we also investigate two kinds of vertical heterostructures $(ZrS_2)_m/(HfS_2)_n$ composed of *m*-layer $ZrS_2$ and *n*-layer $HfS_2$, which are vertically and commensurately stacked. The first one is a V-infinite heterostructure composed of *m*-layer $ZrS_2$ and *n*-layer $HfS_2$ as shown in the inset of Fig.5(a), this stacking sequence repeats periodically and continuously with a 3D hexagonal lattice. The second one is V-finite heterostructure composed of *m* $ZrS_2$ layers continued vertically by a stack of *n* $HfS_2$ layers. Since there are two possible stacking ways (AA and AB) to construct the $(ZrS_2)_m/(HfS_2)_n$ heterostructures (Fig.S3), we compare the total energies of the two V-infinite $(ZrS_2)_1/(HfS_2)_1$ heterostructures and find that AA stacking is more stable than AB stacking by about 35meV. Therefore, we only focus on it in the following vertical heterostructure studies, which should be more preferred under experimental conditions. By changing the number of layers *m* and *n* of the constituent stacks, we can attain different heterostructures, which are also thermally and dynamically stable as shown in Fig. S1(c) and (d). Due to the same lattice symmetry of the monolayers and the $ZrS_2/HfS_2$ heterostructure, the Brillouin zone also remains unchanged[34]. Fig.5(a) shows the projected band structure of the V-infinite $(ZrS_2)_1/(HfS_2)_1$ heterostructure, where the curves highlighted by blue and orange circles are attributed to $ZrS_2$ and $HfS_2$ components, respectively. It is found that the V-infinite structure has an indirect band gap of 1.111eV, which is smaller than both monolayers. It can be seen clearly that the band structures of the constituents are well maintained and separated, the band bending of $ZrS_2$ and $HfS_2$ in the heterostructure is small and the vdW interactions between the $ZrS_2/HfS_2$ layers are weak. The band alignment manifests the intrinsic type-I heterostructure[34]. The band structures of the other V-infinite $(ZrS_2)_m/(HfS_2)_n$ heterostructures are also calculated, where $m=n$, it is found that all the V-infinite $(ZrS2)_m/(HfS_2)_n$ heterostructure possess similar indirect gap nature, and the band gaps decrease very slightly with *m(n)* and the gap nearly keep about 1.05eV as shown in Fig.5(b).

In addition to the V-infinite $(ZrS2)_m/(HfS_2)_n$ heterostructure with the same proportion of building blocks, we also study the $(ZrS2)_m/(HfS_2)_n$ heterostructure with different ratios of components, that is the boundaries have finite width, but are asymmetric. In Fig. 6, the band structures of the asymmetric V-infinite heterostructures $(ZrS_2)_1/(HfS_2)_3$, $(ZrS_2)_1/(HfS_2)_5$ and $(ZrS_2)_1/(HfS_2)_7$ are illustrated. It is impressive that all the asymmetric structures are also indirect bandgap semiconductors, which is different from the Lateral heterostructures $(ZrS2)_m$-$(HfS_2)_n$ [33]. It is also interesting to note that the value of the energy gap is almost

unchanged in the series of consecutive V-infinite heterostructures. The band gaps of the V-infinite heterostructures $(ZrS_2)_m/(HfS_2)_n$ are summarized in Table I, it is shown that there is not so much difference between the bulk materials and most of the considered heterostructures. This is mainly due to the fact that in the heterostructures the intrinsic tensile strain in $HfS_2$ and compressive strain in $ZrS_2$ are very small, where the lattices constant of the heterostructures, bulk $ZrS_2$ and $HfS_2$ are comparable as shown in Table I. While the external strains can provide an effective way to tune the electronic properties and thus enhance the performance of materials [49].

Here we consider the finite size heterostructures composed of *m*-layer $ZrS_2$ stack continued vertically by a stack of *n*-layer $HfS_2$, specified as V-finite $(ZrS_2)_m/(HfS_2)_n$. Fig.7(a) shows the projected band structure of the V-finite structure $ZrS_2/HfS_2$, it is also found that the V-finite heterostructure has an indirect band gap (1.129eV), where the red and blue circles represent the $ZrS_2$ and $HfS_2$ components of the bands, respectively. Fig.7(b) presents the calculated band structures of the other V-finite $(ZrS_2)_m/(HfS_2)_n$ heterostructures, where *m=n.* It is found that all the $(ZrS2)_m/(HfS_2)_n$ heterostructure possess similar indirect gap nature, and the band gaps decrease slightly with *m(n)*.

### 3.2 Optical properties

Our calculated band gaps of the bulk and the monolayer structures are in reasonable agreement with the reported calculated and experimental band gaps [5,50,51]. This suggests that we have a good starting point for the computation of the optical properties. From the dielectric constants, the other optical properties such as the absorption and reflection spectra can be calculated. Because of the sandwich layered properties, $ZrS_2$, $HfS_2$ and the heterostuctures will show highly anisotropic mechanical, optical, and electrical properties[5]. Due to the anisotropy, the dielectric function perpendicular to the layer $\varepsilon_\perp$ is different from $\varepsilon_\parallel$ that is parallel to the layer. The real and imaginary parts of the energy-dependent dielectric functions are calculated at PBE level. All the imaginary parts of the dielectric function of the bulk, monolayer and the heterostructures are calculated (not show here), in Fig.S4 we just show the imaginary parts of the dielectric function of the $ZrS_2$ bulk and monolayer. It is shown that the imaginary parts of $\varepsilon_\parallel$ dominate in the lower energy region (0 to 4 eV), both $\varepsilon_\parallel$ and $\varepsilon_\perp$ contribute in the higher energy region (above 4 eV).

The real part could be obtained through Kramers–Kronig relations [41], the results of bulk $ZrS_2$, bulk $HfS_2$, monolayer $ZrS_2$ and monolayer $HfS_2$ are illustrated in Fig. 8. Strong anisotropy is observed between

the real parts of dielectric functions $\varepsilon_{\parallel}$ and $\varepsilon_{\perp}$. It is found that the real part of $\varepsilon_{\parallel}$ of bulk $ZrS_2$(bulk $HfS_2$) is negative between 2.54 eV and 2.86 eV (2.74 eV and 3.30 eV), while $\varepsilon_{\perp}$ is positive, leading to a hyperbolic region (based on the criterion Real ($\varepsilon_{\parallel}$)<0) in which the two components have different signs (marked as the blue shaded regions in Fig. 8). This sign difference is the characteristic feature of so-called indefinite media[18,19], which was proposed in the study of metamaterials and has important potential applications such as near-field focusing and spontaneous emission enhancement [20,21,52,53]. The bulk materials exhibit predominantly type II dispersion corresponding to metallic response in-plane and dielectric response out-of-plane [20]. The strong dielectric anisotropy should arise from the weak interlayer coupling that lowers carrier velocities and plasma frequencies perpendicular to the layers. For the monolayer $ZrS_2$ and monolayer $HfS_2$, they exhibit anisotropic dielectric properties. In order to predict accurate dielectric function, HSE06 hybrid exchange-correlation functional is utilized to calculate the bulk $ZrS_2$. We compared the dielectric function of bulk $ZrS_2$ obtained with the PBE and HSE06 in Fig.S4 (c), where the real parts of $\varepsilon_{\parallel}$ and $\varepsilon_{\perp}$ are plotted. It is found that there are some blueshifts in the hyperbolic window from 2.54 - 2.86 eV (PBE) to 3.34 - 3.56 eV (HSE06) for $ZrS_2$ bulk. Although PBE calculation is expected to influence the precise position of the hyperbolic regions, the calculated results are reasonable to reflect the hyperbolic property. And the more accurate method such as hybrid functional and DFT+U approach deserve to be investigated for the proposed heterostructures in future research.

For the lateral heterostructures, optical bianisotropy , for in-plane and out-of-plane directions, will be described by the dielectric tensor with three different components. $\varepsilon_{\parallel}(\varepsilon_{xx}, \varepsilon_{yy})$ and $\varepsilon_{\perp}(\varepsilon_{zz})$ of the periodic lateral heterostructure $(ZrS_2)_1$-$(HfS_2)_1$ and $(ZrS_2)_4$-$(HfS_2)_4$ are calculated in Fig.9. It is found that lateral heterostructure $(ZrS_2)_1$-$(HfS_2)_1$ does not exhibit hyperbolic region, while $(ZrS_2)_4$-$(HfS_2)_4$ possesses a hypobolic region between between 2.7 eV and 3.02 eV, where $\varepsilon_{xx}<0$, $\varepsilon_{yy}<0$ and $\varepsilon_{zz}>0$. The metallic response in-plane may come from the strong coupling between different constituents.

From the charge distribution and the charge density difference in $(ZrS_2)_m/(HfS_2)_n$ VHs, it is found that the charges mainly distribute in the respective monolayer, whereas only a few charges will transfer at the interface. Hence, the dielectric response in parallel direction can be determined by the respective material. Although the vdW interactions existing between the layers of the $ZrS_2/HfS_2$ heterostructure are weak, the interfaces play important role in the scattering for electrons moving perpendicular to the interface and affect

the perpendicular part of the optical dielectric functions. Fig.10(a) shows the calculated $\varepsilon_{\perp}$ of the V-infinite heterostructures $(ZrS_2)_1/(HfS_2)_1$, $(ZrS_2)_3/(HfS_2)_3$, $(ZrS_2)_6/(HfS_2)_6$ and $(ZrS_2)_9/(HfS_2)_9$, where the shaded region shows the hyperbolic region. It is clear that all the V-infinite heterostructures possess a hyperbolic region between 2.7 eV and 3.02 eV. For comparison, we also calculated different V-infinite heterostructures $(ZrS_2)_m/(HfS_2)_n$ with $m=n$ as shown in Fig.10 (b), it is found that when $m=n$ , the hyperbolic regions are nearly the same. The hyperbolic character of the vertical heterostructure arise from the combination of the $ZrS_2$ and $HfS_2$, which is different from the dielectric property of the respective pristine $ZrS_2$ and $HfS_2$ bulk. Importantly, changes in the constituent ratio, *m/n*, result in tuning of the hyperbolic region. Fig.10 (c) shows the calculated $\varepsilon_{\perp}$ of the V-infinite heterostructures $(ZrS_2)_1/(HfS_2)_3$ and $(ZrS_2)_1/(HfS_2)_5$, the position and width of the hyperbolic region changes with the ratio of *m/n*. The hyperbolic dielectric properties of the V-infinite heterostructures $(ZrS_2)_m/(HfS_2)_n$ are summarized in Table I. To illustrate the degree of tuning that can be achieved by vdW heterostructures with different $ZrS_2$ and $HfS_2$ layers, we apply effective medium theory (EMT) to calculate the permittivity of the V-infinite heterostructures $(ZrS_2)_m/(HfS_2)_n$ with different thickness ratio, $d_{HfS2}/d_{ZrS2}$. Where the thicknesses of the $ZrS_2$ and $HfS_2$ layers are sufficiently sub-wavelength. It should be noticed that the influence of hybridization at the interfaces and quantum confinement are neglected in this calculation [18].

In EMT, a uniaxial stratified periodic metamaterial consisting of $ZrS_2$ and $HfS_2$ layers can be characterized by the effective diagonal permittivity tensor $\varepsilon^{EMT} = diag(\varepsilon_{//}^{EMT}, \varepsilon_{//}^{EMT}, \varepsilon_{\perp}^{EMT})$ with effective components given by [19] $\varepsilon_{//}^{EMT} = \rho \cdot \varepsilon_{//}^{HfS_2} + (1-\rho) \cdot \varepsilon_{//}^{ZrS_2}$ , $1/\varepsilon_{\perp}^{EMT} = \rho / \varepsilon_{\perp}^{HfS_2} + (1-\rho)/\varepsilon_{\perp}^{ZrS_2}$ ,where $\rho = d_{HfS_2}/(d_{ZrS_2} + d_{HfS_2})$ is the fill fraction of $HfS_2$. Fig.10(d) shows that the hyperbolic energy region can be tunable, over which the heterostructure dispersion is hyperbolic. By choosing V-infinite heterostructures with different $ZrS_2$ and $HfS_2$ layers, the hyperbolic region can be adjusted. For comparison the calculated DFT data $\varepsilon_{\perp}$ (for $(ZrS_2)_1/(HfS_2)_1$, $(ZrS_2)_1/(HfS_2)_3$ and $(ZrS_2)_1/(HfS_2)_5$) are also plotted in Fig.10(d). The V-infinite heterostructures are hyperbolic in the ranges 2.750 - 3.038 eV, 2.745 - 3.168 eV and 2.745 - 3.197 eV, respectively, which are in good agreement with the EMT results. For the TMDs heterostructure-based HMMs, EMT can be effective in evaluating the hyperbolic regime where real($\varepsilon_{\perp}$)<0. Further tuning is obviously possible by considering heterostructures with other 2D material or metal [52]. In addition, the hyperbolic dispersion property are also found in the V-finite heterostructures $(ZrS_2)_m/(HfS_2)_n$. In the

hyperbolic region, the surfaces of constant frequency are hyperbolic, extending to very large values of *k*. Because of the momentum mismatch, the naturally HMMs will possess large local density of states [21, 53] and are expected to deliver high Purcell enhancements.

### 3.3 Purcell enhancement

One of the most promising applications of hyperbolic metamaterials is spontaneous emission engineering, which plays a crucial role in single photon sources and light-emission devices [21, 54]. Due to the hyperbolic dispersion, a dipole emitter can couple to a large range of *k*-states at a single frequency, thereby increasing the number of possible decay paths. The Purcell factor is generally defined as the ratio of the radiative rate in a particular electromagnetic structure to that in vacuum, it is an efficient parameter to characterize the spontaneous emission properties, which describes the modification of the spontaneous emission lifetime [53]. In contrast to resonant structures like cavities or single metallic interfaces, the HMM exhibit a Purcell factor that is broadband and tunable in frequency [21]. To study the spontaneous emission enhancement of a point source above such ($ZrS_2$)/($HfS_2$) multilayer HMMs, Purcell factors are computed. For simplicity an ideal electric dipoles with internal quantum efficiency $q_0$=1 is adopted. When a dipole is placed at a distance of *d* above the planar HMM with polarization perpendicular ($\perp$) or parallel ($/\!/$) to the interface, the corresponding Purcell factors can be written as [53, 55]

$F_{p\perp} = 1 - q_0 + \frac{3}{2} q_0 \,\mathrm{Re} \int_0^\infty \frac{1}{k_z} (\frac{k_x}{\sqrt{\varepsilon_1} k_0})^3 (1 + r_p e^{2ik_z d}) dk_x$ and

$F_{p\perp} = 1 - q_0 + \frac{3}{4} q_0 \,\mathrm{Re} \int_0^\infty \frac{1}{k_z} \frac{k_x}{\sqrt{\varepsilon_1} k_0} [1 + r_s e^{2ik_z d} + \frac{k_z^2}{\varepsilon_1 k_0^2} (1 - r_p e^{2ik_z d}) dk_x$, where $k_0$ is the magnitude of the wave vector in a vacuum, $\varepsilon_1$ is the relative permittivity for the host material which contains fluorescent emitters such as quantum dots and dye molecules, $k_x$ and $k_z = \sqrt{\varepsilon_1 k_0^2 - k_x^2}$ are the wavevector components along the in-plane and vertical directions respectively and $r_{p,s}$ is the reflection coefficient at the interfaces for a TM (TE) polarized wave, which can be calculated by transfer matrix method [56]. The isotropic Purcell factor $F_{\mathrm{iso}}$ can be obtained through an average over $F_{p\perp}$ and $F_{p//}$, that's $F_{iso} = \frac{1}{3} F_{p\perp} + \frac{2}{3} F_{p//}$, where the factor 2 accounts for the two equivalent orthogonal in-plane orientations.

Fig.11(a) shows the Purcell factor for the dipoles perpendicular ($F_{p\perp}$, short dotted line) and parallel ($F_{p//}$, short dashed line) to the V-infinite ($ZrS_2$)/($HfS_2$) heterostructure surface with $d_{HMM}$=20nm as depicted in the

inset, the solid line represents the Purcell factor $F_{iso}$ for an isotropic dipole which is averaged from $F_{p\perp}$ and $F_{p//}$. The distance between dipole and the $(ZrS_2)/(HfS_2)$ heterostructure HMM is $d$=5 nm and $\varepsilon_1 = 1$. The permittivity of the naturally HMM calculated by DFT is shown in Fig.S5, around 450 nm, where $\varepsilon_{//}<0$, the dispersion relation is hyperbolic. The peak of the Purcell factor is located at the 300-650nm wavelength region which might result from the larger local density of states around the hyperbolic region, and the Purcell factor $F_{p\perp}$ is much higher than $F_{p//}$. About 102-fold enhancement at $\lambda$ =405 nm is obtained. Fig.11(b) shows the Purcell factor $F_{p\perp}$ as a function of wavelength with different $d$ and $\varepsilon_1$. Apparently, the Purcell factor relates to the distance between the dipole and the $(ZrS_2)/(HfS_2)$ heterostructure and the host materials. The Purcell factor decreases with the coupling distance $d$ and the permittivity of the host materials.

**4. Conclusion**

In summary, we have studied the electronic and optical dielectric properties of the lateral and vertical heterostructures composed of $ZrS_2$ and $HfS_2$ mono and multilayer. It is found that both the monolayer and the bulk structures are intrinsic indirect semiconductors, while the lateral heterostructures $(ZrS_2)_m$-$(HfS_2)_n$ exhibit an indirect to direct bandgap transition. The optical properties of the $HfS_2$ and $ZrS_2$ bulk and monolayers are found to be strongly anisotropic. The bulk $HfS_2$ and $ZrS_2$ are naturally hyperbolic metamaterial between 2.54 eV and 2.86 eV (2.74 eV and 3.30 eV) respectively. The periodic and finite size vertical heterostructures $(ZrS_2)_m/(HfS_2)_n$ keep the indirect bandgap property. The vertical heterostructures possess tunable hyperbolic dielectric behavior and the property can be well predicted by the effective medium theory, where the interface effects are not crucial. While the heterostructures with non-negligible interface effects deserve to be investigated next step. Furthermore, in the hyperbolic region over a 100-fold Purcell factor enhancement is obtained, presenting a promising opportunity for the realization of hyperbolic metamaterial-based devices for light-generation.

**Acknowledgements**

L. Z would like to thank Dr. P. Cencillo-Abad at NanoScience Technology Center, University of Central Florida (USA) for helpful advice in revising this paper. This research was supported by National Natural Science Foundation of China (Grants No. U1804165, No. U1604133, No. 11804081 and No. 11804082) and by Natural Science Foundation of Henan Province (Grants No. 15A416007, No. NSFRF140132 and No. 182102410047).

## References


[1] S. Manzeli, D. Ovchinnikov, D. Pasquier, O. V. Yazyev, and A. Kis, Nat. Rev. Mater. **2**, 17033 (2017).

[2] P. Liu and B. Xiang, Sci. Bull. **62**, 1148 (2017).

[3] S. Dai, Q. Ma, M. Liu, T. Andersen, Z. Fei, M. Goldflam, M. Wagner, K. Watanabe, T. Taniguchi, M. Thiemens., Nat. nanotechnol.**10**, 682 (2015).

[4] A. A. Tedstone, D. J. Lewis, and P. O'Brien, Chem. Mater. **28**, 1965 (2016).

[5] Q. Zhao, Y. Guo, K. Si, Z. Ren, J. Bai, and X. Xu, Phys. Status Solidi B **254**, 1700033 (2017).

[6] W. Choi, N. Choudhary, G. H. Han, J. Park, D. Akinwande, and Y. H. Lee, Mater. Today **20**, 116 (2017).

[7] F. Zheng and J. Feng, Phys. Rev. B **99**, 161119 (2019).

[8] A. K. Geim and I. V. Grigorieva, Nature **499**, 419 (2013).

[9] Z. Ji, H. Hong, J. Zhang, Q. Zhang, W. Huang, T. Cao, R. Qiao, C. Liu, J. Liang, C. Jin, ACS nano **11**, 12020 (2017).

[10] Z. Wang, Y. Xie, H. Wang, R. Wu, T. Nan, Y. Zhan, J. Sun, T. Jiang, Y. Zhao, Y. Lei, Nanotechnology **28**, 325602 (2017).

[11] H. Taghinejad, A. A. Eftekhar, and A. Adibi, Opt. Mater. Express **9**, 1590 (2019).

[12] E. Pomerantseva and Y. Gogotsi, Nat. Energy **2**, 17089 (2017).

[13] V. D. S. O. Ganesan, J. Linghu, C. Zhang, Y. P. Feng, and L. Shen, Appl. Phys. Lett. **108**, 122105 (2016).

[14] L. Li, H. Wang, X. Fang, T. Zhai, Y. Bando, and D. Golberg, Energ. Environ. Sci. **4**, 2586 (2011).

[15] M. Zhang, Y. Zhu, X. Wang, Q. Feng, S. Qiao, W. Wen, Y. Chen, M. Cui, J. Zhang, C. Cai, L. Xie, J. Am. Chem.Soc. **137**, 7051 (2015).

[16] T. Kanazawa, T. Amemiya, A. Ishikawa, V. Upadhyaya, K. Tsuruta, T. Tanaka, and Y. Miyamoto, Sci Rep-Uk **6**, 22277 (2016).

[17] A. Onen, D. Kecik, E. Durgun, and S. Ciraci, The Journal of Physical Chemistry C **121**, 27098 (2017).

[18] M. N. Gjerding, R. Petersen, T. Pedersen, N. A. Mortensen, and K. S. Thygesen, Nat. Commun. **8**, 320 (2017).

[19] A. Poddubny, I. Iorsh, P. Belov, and Y. Kivshar, Nat Photonics **7**, 948 (2013).

[20] L. Ferrari, C. H. Wu, D. Lepage, X. Zhang, and Z. W. Liu, Progress In Quantum Electronics **40**, 1 (2015).

[21] D. Lu, J. J. Kan, E. E. Fullerton, and Z. Liu, Nat. nanotechnol. **9**, 48 (2014).

[22] Y.-L. Liao, Y. Zhao, S. Wu, and S. Feng, Opt. Mater. Express **8**, 2484 (2018).

[23] A. P. Slobozhanyuk *et al.*, Phys. Rev. B **92**, 195127 (2015).

[24] O. Kidwai, S. V. Zhukovsky, and J. Sipe, Phys. Rev. A **85**, 053842 (2012).

[25] P. Shekhar, S. Pendharker, D. Vick, M. Malac, and Z. Jacob, Opt. express **27**, 6970 (2019).

[26] J. D. Caldwell, A.V. Kretinin, Y. Chen, V. Giannini, M.M. Fogler, Y. Francescato, C.T. Ellis, J.G. Tischler, C.R. Woods, A.J. Giles, Nat. Commun. **5**, 5221 (2014).

[27] E. E. Narimanov and A. V. Kildishev, Nat. Photonics **9**, 214 (2015).

[28] Z. Liu and K. Aydin, Nano Lett **16**, 3457 (2016).

[29] H. Qi, L. Wang, J. Sun, Y. Long, P. Hu, F. Liu, and X. He, Crystals **8**, 35 (2018).

[30] R. Dong and I. Kuljanishvili, J. Vac. Sci. Technol. B **35**, 030803 (2017).

[31] K. Novoselov, A. Mishchenko, A. Carvalho, and A. C. Neto, Science **353**, aac9439 (2016).

[32] A. Onen, D. Kecik, E. Durgun, and S. Ciraci, Phys. Rev. B **95**, 155435 (2017).

[33] J. Yuan, N. Yu, J. Wang, K.-H. Xue, and X. Miao, Appl. Surf. Sci. **436**, 919 (2018).

[34] J. Shang, S. Zhang, X. Cheng, Z. Wei, and J. Li, RSC Adv. **7**, 14625 (2017).

[35] P. E. Blöchl, Phys. Rev. B **50**, 17953 (1994).

[36] G. Kresse and J. Furthmüller, Phys. Rev. B **54**, 11169 (1996).

[37] J. P. Perdew, K. Burke, and M. Ernzerhof, Phys. Rev. Lett. **77**, 3865 (1996).

[38] H. J. Monkhorst and J. D. Pack, Phys. Rev. B **13**, 5188 (1976).

[39] S. Grimme, J. Comput. Chem. **27**, 1787 (2006).

[40] M. Gajdoš, K. Hummer, G. Kresse, J. Furthmüller, and F. Bechstedt, Phys. Rev. B **73**, 045112 (2006).

[41] V. Lucarini, J. J. Saarinen, K.-E. Peiponen, and E. M. Vartiainen, Kramers-Kronig relations in optical materials research (Springer Science & Business Media, 2005).

[42] Y. Li, J. Kang, and J. Li, RSC Adv. **4**, 7396 (2014).

[43] A. Kumar and P. Ahluwalia, Eur. Phys. J. B **85**, 186 (2012).

[44] Q. Sun, Y. Dai, Y. Ma, W. Wei, and B. Huang, RSC Adv. **5**, 33037 (2015).

[45] See Supplemental Material at http: for the phonon dispersion and the molecules dynamic of the lateral heterostructure and vertical heterostructure, the band structures of $(ZrS_2)_3$-$(HfS_2)_3$ and the superlattice $(ZrS_2)_2$-$(ZrS_2)_2$, and the dielectric functions of the $ZrS_2$ bulk, monolayer and V-infinite $(ZrS_2)$/$(HfS_2)$ heterostructure.

[46] Q. Wang, P. Wu, G. Cao, and M. Huang, J. Phys. D: Appl. Phys. **46**, 505308 (2013).

[47] Q. Sun, Y. Dai, Y. Ma, N. Yin, W. Wei, L. Yu, and B. Huang, 2D Materials **3**, 035017 (2016).

[48] J. Heyd, G. E. Scuseria, and M. Ernzerhof, J. Chem. Phys. **118**, 8207 (2003).

[49] N. L. Hongyan Guo, Lu Wang, Xiaojun Wu, and Xiao Cheng Zeng, J.Phys. Chem. C **118**, 7242 (2014).

[50] Y. Zhu, X. Wang, M. Zhang, C. Cai, and L. Xie, Nano Res. **9**, 2931 (2016).

[51] F. A. R. a. K. S. Thygesen, J. Phys. Chem. C **119**, 13169 (2015).

[52] X. Song, Z. Liu, Y. Xiang, and K. Aydin, Opt. express **26**, 5469 (2018).

[53] L. Li, W. Wang, T. S. Luk, X. Yang, and J. Gao, ACS Photonics **4**, 501 (2017).

[54] S. Axelrod, M. K. Dezfouli, H. M. Wong, A. S. Helmy, and S. Hughes, Phys. Rev. B **95**, 155424 (2017).

[55] G. W. Ford and W. H. Weber, Phys. Rep. **113**, 195 (1984).

[56] L. Zhang, W. Yu, J.-Y. Ou, Q. Wang, X. Cai, B. Wang, X. Li, R. Zhao, and Y. Liu, Phys. Rev. B **98**, 075434 (2018).

# Figures and Figure captions

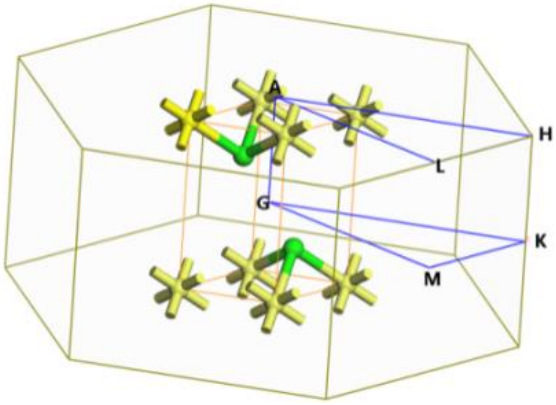


Fig.1 The Brillouin zone with high symmetry K-points used in band structure calculations, where 1T-$MX_2$ (M=Zr, Hf; X= S) unit cell structure is also shown, the green and yellow spheres denote M and S atoms, respectively.

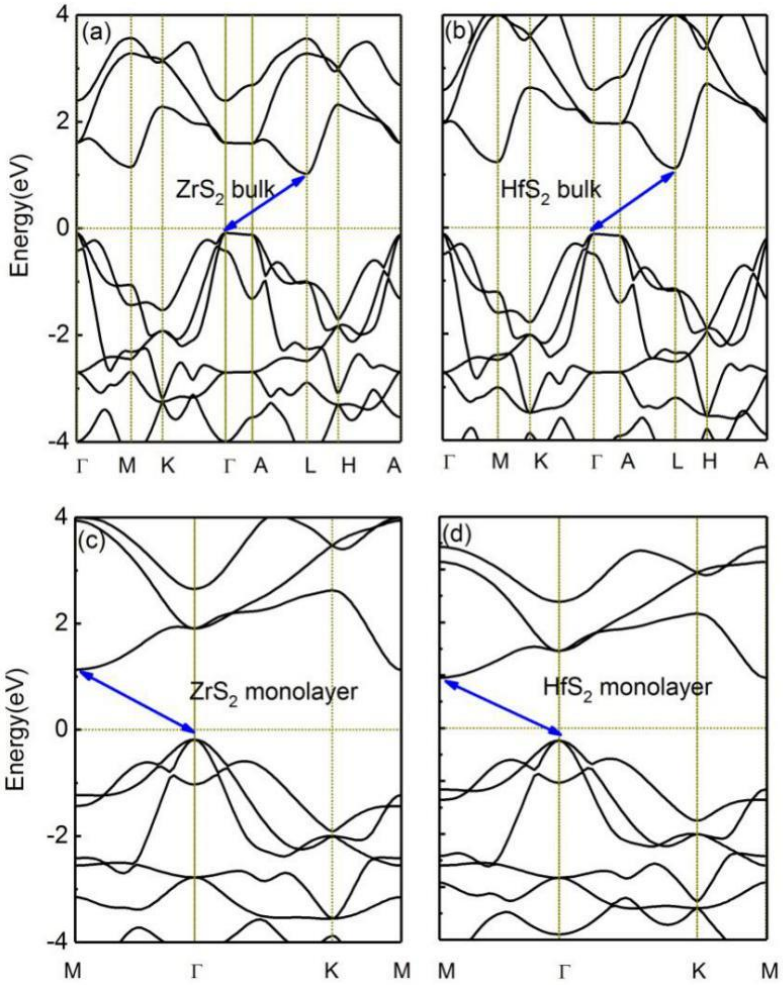


Fig.2 Band structures of bulk $ZrS_2$, bulk $HfS_2$, $ZrS_2$ monolayer and $HfS_2$ monolayer. The blue arrows indicate the bandgaps and the horizontal dashed lines represent the Fermi level.

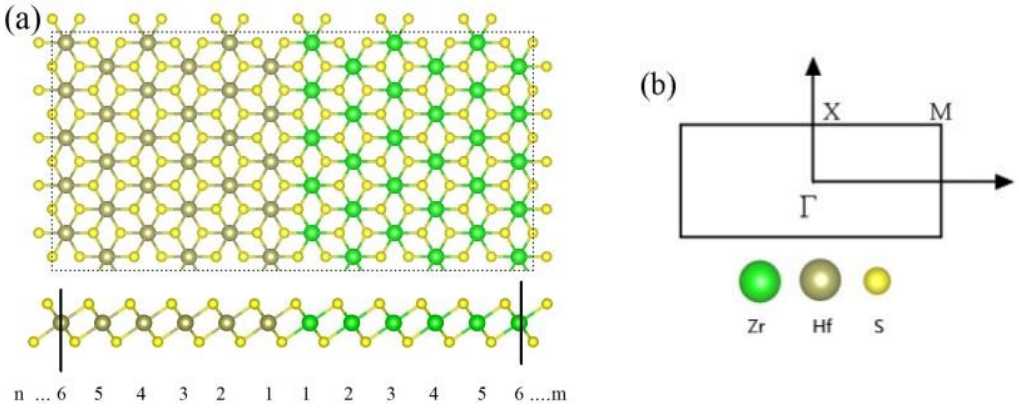


Fig.3 Top and side views of atomic configurations of $(ZrS_2)_m$-$(HfS_2)_n$ lateral heterostructure monolayers with zigzag interlines, where $m$=6 and $n$=6. Green, sand and yellow balls indicate Zr, Hf, and S atoms, respectively. (b) 2D Brillouin zone of the monolayer LH with high symmetry points.

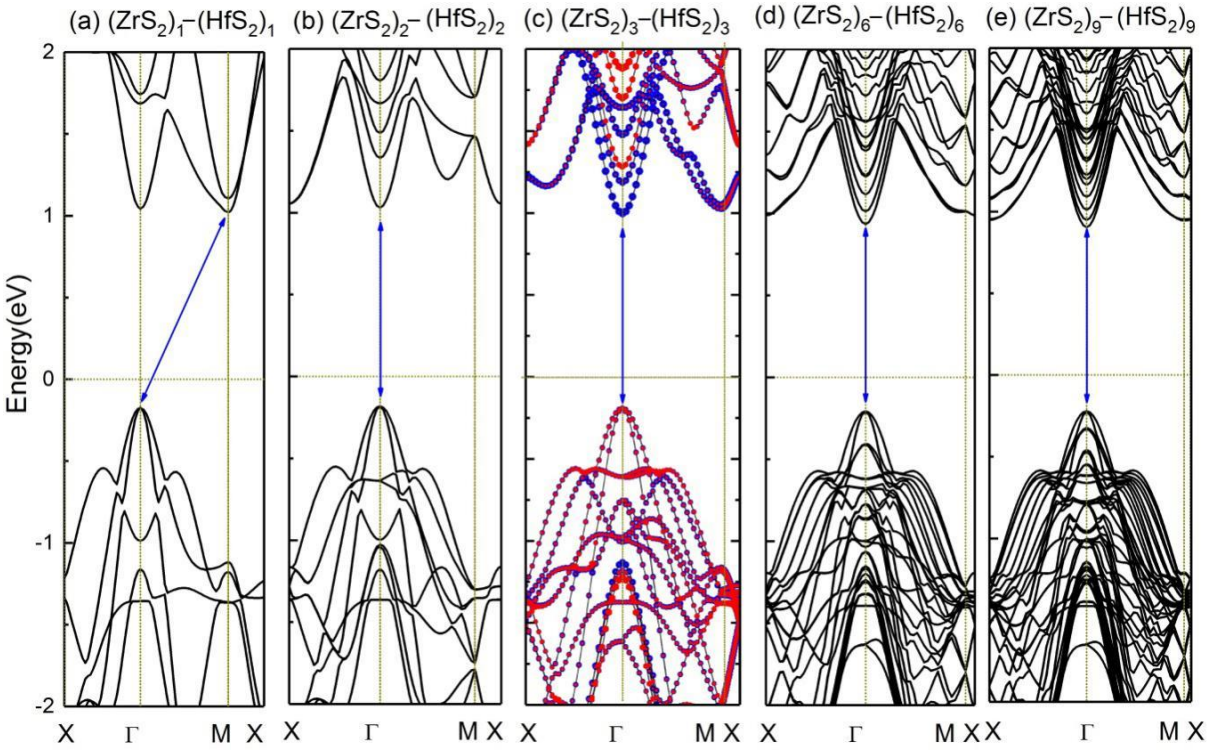


Fig.4 The calculated band structures of the periodic lateral heterostructures $(ZrS_2)_m$-$(HfS_2)_n$ at PBE level. (a) $(ZrS_2)_1$-$(HfS2)_1$, (b) $(ZrS_2)_2$-$(HfS2)_2$, (c) $(ZrS_2)_3$-$(HfS2)_3$, (d) $(ZrS_2)_6$-$(HfS_2)_6$ and (e) $(ZrS2)_9$-$(HfS2)_9$, where (c) is the calculated projected band structure, the blue and red line represent the $ZrS_2$ and $HfS_2$ components of the bands, respectively. The blue arrows indicate the bandgaps and the horizontal dashed lines represent the Fermi level.

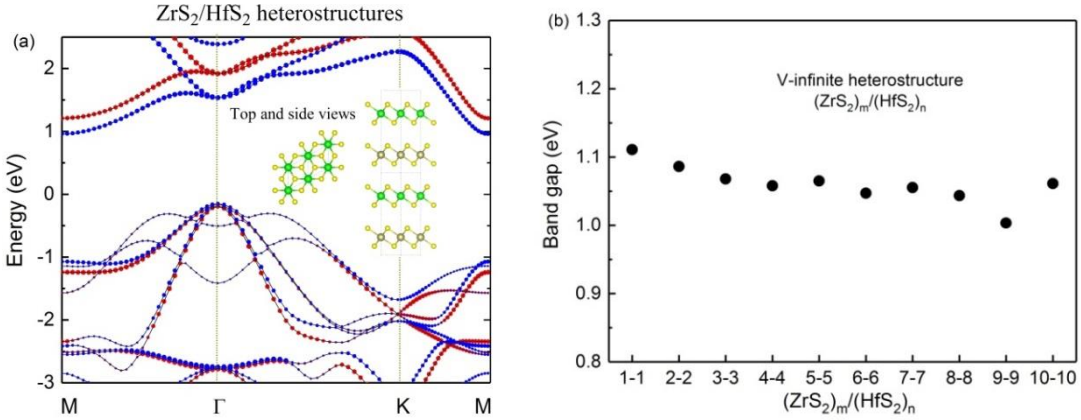


Fig.5 The calculated projected band structure of the V-infinite heterostructures $(ZrS_2)_1/(HfS_2)_1$, the top and side views of the AA stacking heterostructure are shown in the inset. (b) The bandgap of different V-infinite heterostructures $(ZrS_2)_m/(HfS_2)_n$, where $m$=$n$ is an integer.

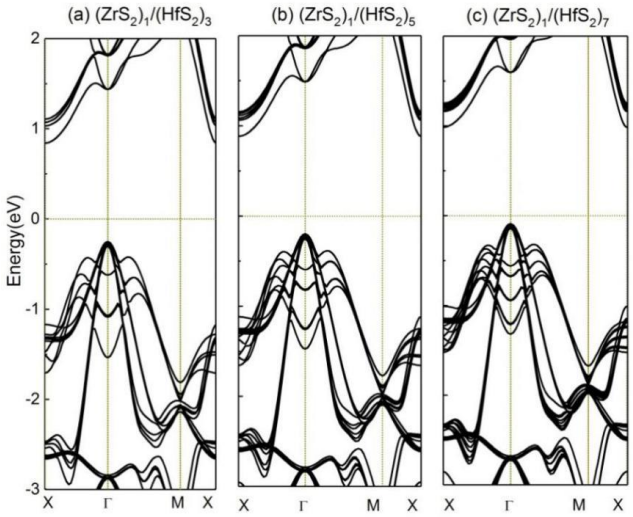


Fig.6 The calculated band structures of the V-infinite heterostructures $(ZrS_2)_1/(HfS_2)_3$ (a), $(ZrS_2)_1/(HfS_2)_5$ (b) and $(ZrS_2)_1/(HfS_2)_7$ (c), respectively.

Table I. The lattice constants (a), band gaps and hyperbolic dielectric properties of the V-infinite heterostructures $(ZrS_2)_m/(HfS_2)_n$, it is also found that all the V-infinite heterostructures keep the indirect bandgap property and possess a hyperbolic dielectric behavior.

| Heterostructure $(ZrS_2)_m/(HfS_2)_n$ | $m$=1 $n$=1 | $m$=1 $n$=3 | $m$=1 $n$=5 | $m$=2 $n$=2 | $m$=3 $n$=3 | $m$=4 $n$=4 | $m$=5 $n$=5 | $m$=6 $n$=6 | $m$=7 $n$=7 | $m$=8 $n$=8 | $m$=9 $n$=9 | $m$=10 $n$=10 |
|---|---|---|---|---|---|---|---|---|---|---|---|---|
| lattice constant a (Å) | 3.664 | 3.654 | 3.651 | 3.664 | 3.664 | 3.663 | 3.664 | 3.664 | 3.664 | 3.661 | 3.664 | 3.664 |
| Band gap(eV) | 1.111 | 1.0909 | 1.0821 | 1.0863 | 1.0681 | 1.0581 | 1.0652 | 1.0471 | 1.0553 | 1.0436 | 1.0034 | 1.0611 |
| Hyperbolic window(eV) | 0.2866 | 0.4218 | 0.4505 | 0.3067 | 0.2978 | 0.3083 | 0.2994 | 0.3166 | 0.3134 | 0.349 | 0.3548 | 0.3501 |

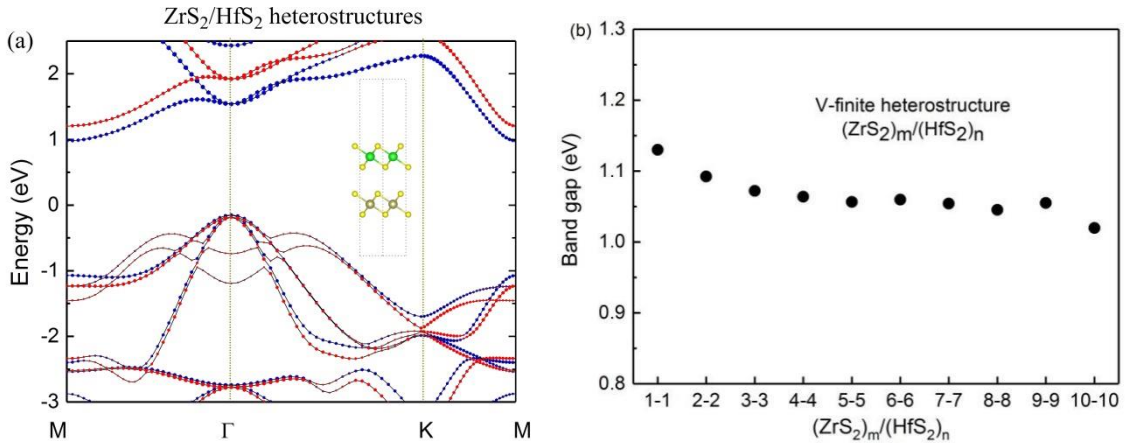


Fig.7 The calculated projected band structure of the V-finite heterostructures $(ZrS_2)_1/(HfS_2)_1$ constructed by $ZrS_2$ and $HfS_2$ monolayer, the inset shows the side views of the AA stacking heterostructures. (b) The band gap of different V-finite heterostructures $(ZrS_2)_m/(HfS2)_n$ formed by thin stacks of $ZrS_2$ and $HfS_2$.

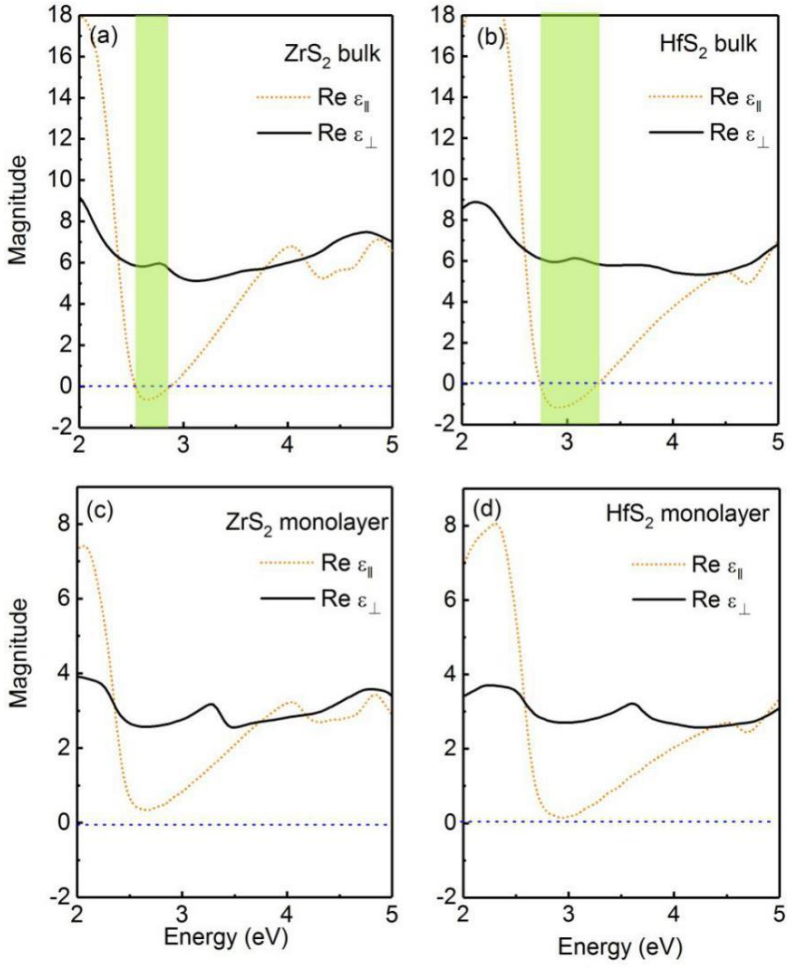


Fig.8 Real parts of the two principal components of permittivity of bulk $ZrS_2$, bulk $HfS_2$, monolayer $ZrS_2$ and monolayer $HfS_2$, respectively, where $\varepsilon_{\parallel}$ represents in-plane component and $\varepsilon_{\perp}$ represents out-of-plane component. The shaded region shows the hyperbolic regions.

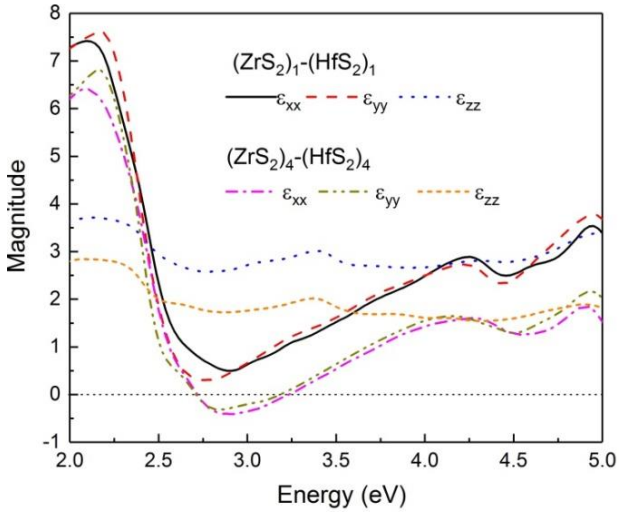


Fig.9 Real parts of $\varepsilon_{\parallel}$ ($\varepsilon_{xx}$, $\varepsilon_{yy}$) and $\varepsilon_{\perp}$($\varepsilon_{zz}$) of the periodic lateral heterostructures $(ZrS_2)_1$-$(HfS_2)_1$ and $(ZrS_2)_4$-$(HfS_2)_4$, respectively.

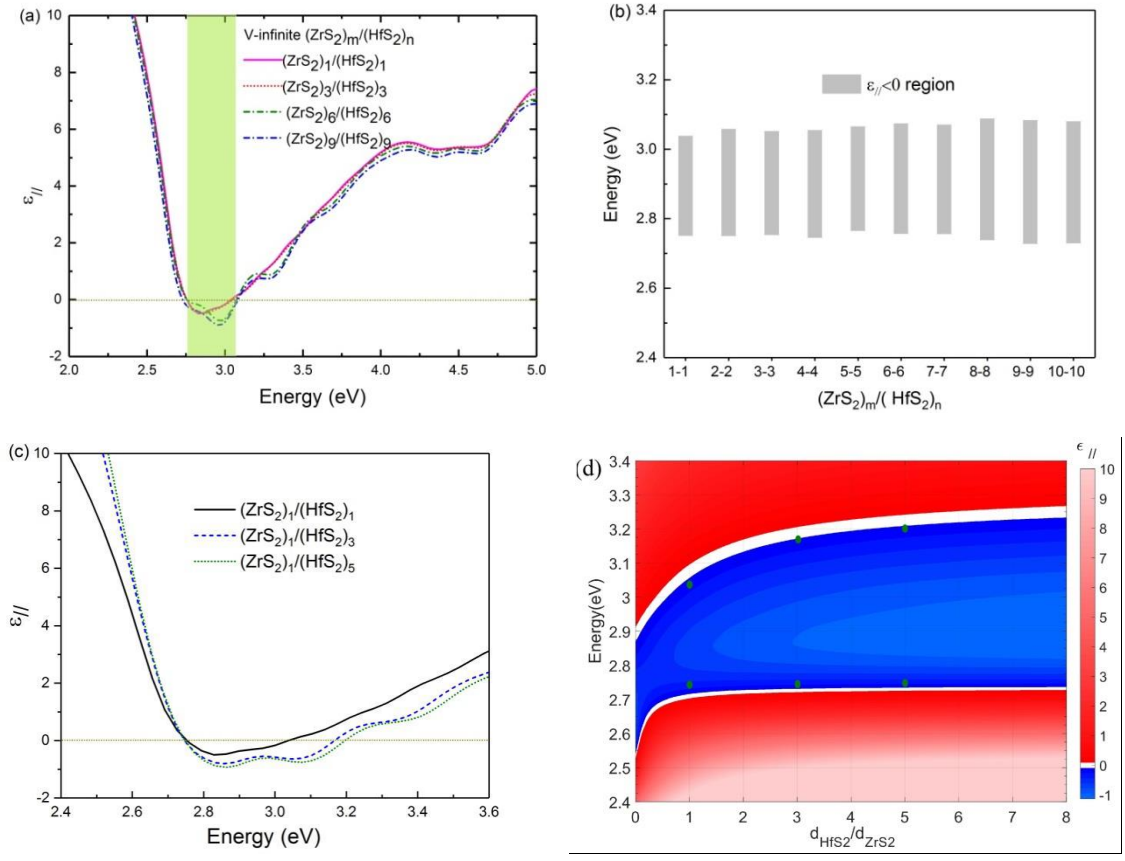


Fig.10 $\varepsilon_{\parallel}$ of the V-infinite heterostructure $(ZrS_2)_1/(HfS_2)_1$, $(ZrS_2)_3/(HfS_2)_3$, $(ZrS_2)_6/(HfS_2)_6$ and $(ZrS_2)_9/(HfS_2)_9$(a), where the shaded region shows the hyperbolic regions. (b) the hyperbolic regions of different V-infinite heterostructures $(ZrS_2)_m/(HfS_2)_n$. (c) $\varepsilon_{\parallel}$ of the V-infinite heterostructure $(ZrS_2)_1/(HfS_2)_3$ and $(ZrS_2)_1/(HfS_2)_5$, for comparison, $\varepsilon_{\parallel}$ of $(ZrS_2)_1/(HfS_2)_1$ is also plotted. (d) The effective $\varepsilon_{\parallel}$ of the composited $ZrS_2/HfS_2$ materials with different thickness ration based on EMT, where the olive dots represent the calculated zeros of $\varepsilon_{\parallel}$ for $(ZrS_2)_1/(HfS_2)_1$, $(ZrS_2)_1/(HfS_2)_3$ and $(ZrS_2)_1/(HfS_2)_5$, respectively.

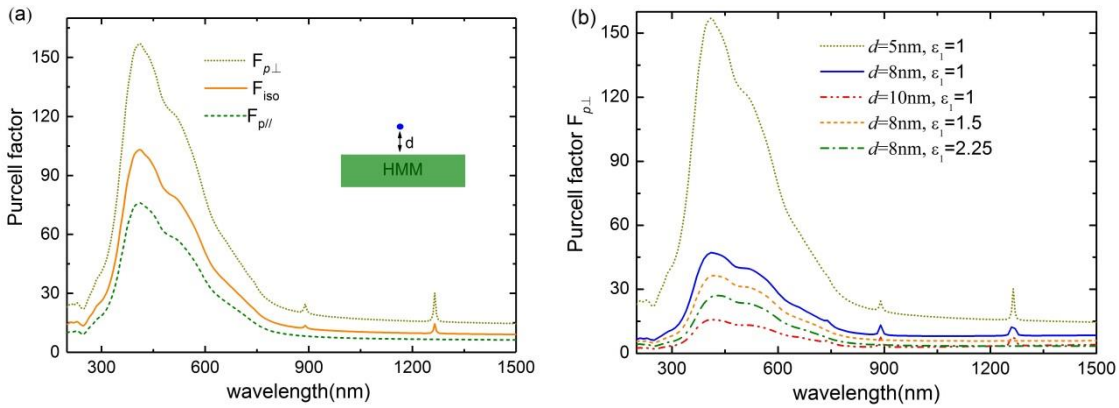


Fig.11(a) Purcell factor for the dipoles perpendicular ($F_{p\perp}$, short dotted line) and parallel ($F_{p//}$, short dashed line) to the surface as depicted in the insets (the blue dot represents a dipole), the solid line represents the Purcell factor $F_{iso}$ for an isotropic dipole which is averaged from $F_{p\perp}$ and $F_{p//}$. The dipole is in air 5 nm above the $(ZrS_2)/(HfS_2)$ multilayer HMM with $d_{HMM}$=50 nm. (b) Purcell factor $F_{p\perp}$ as a function of wavelength with different $d$ and $\varepsilon_1$.